Research Article

Journal of Environmental Nanotechnology

Investigation of $BaZrO_3$ Nanoparticles for Photocatalytic Activity and the Effects of Y-doping

C. Chinnusamy and R. Thiyagarajan*
PG & Research Department of Physics, Chikkaiah Naicker College, Erode, TN, India
Received: 22.07.2024 Accepted: 13.09.2024 Published: 30.09.2024
*thiyaguphyxics@gmail.com

ABSTRACT

A straightforward co-precipitation technique with yttrium doping (X = 0, 0.02, 0.04, 0.06) was used to fabricate perovskite $Ba_{1-x}Y_xZrO_3$ nanoparticles. Employing Powder X-ray diffraction (PXRD) technique, the compound was characterized and found to have a perovskite structure crystallized in a cubic lattice. Images from scanning electron microscopy (SEM) show plenty of pores between the grains and a structure resembling a rod. The purity and formation of B-site in the nanostructure was confirmed by a Fourier Transform Infrared (FT-IR) spectrophotometer. The UV-Vis profile and photoluminescence (PL) spectra of the powder were also ascertained. Using methylene blue as a model organic pollutant, the powder as a photocatalyst was tested for two hours under UV light irradiation. The Y-doped nanoparticles broke down the dye by ~98.5% at pH = 8 when exposed to UV light. The enhanced photocatalytic performance exhibited by Y-doped $BaZrO_3$ nanoparticles can be attributed to their efficient charge separation and increased adsorption capabilities by the presence of $BaZrO_3$.

Keywords: Perovskite; Photocatalytic degradation; Zirconium-based nanoparticles; Yttrium doping.

1. INTRODUCTION

Environmental pollution has increased dramatically over the last few years. Hazardous chemical-laden industrial wastes can contaminate water, posing a threat to human health by interfering with photosynthetic activity, reducing soil fertility, influencing crop productivity, poisoning aquatic life, and triggering serious illnesses like allergies and skin cancer. The potential risks associated with contaminated waterways have increased significantly due to the release of various textile organic dyes into freshwater streams, which generate wastewater. Because the demand for drinkable water is growing, contaminated water needs to be treated to make it safe to drink (Fujishima *et al.* 1972; Yuan *et al.* 2016; Yin *et al.* 2019).

Photocatalysis, which produces carbon dioxide and water molecules as its end products, is a cheap and efficient way to rid water of different organic pollutants. Based on thiazine, methylene blue (MB) is an azo dye with a cationic complex structure. Treating contaminated water that contains MB dye is difficult because of its complex cationic structure, which stops the dye from degrading.

Water is contaminated by metal oxide-based photocatalysts, which eliminate dangerous substances like organic dyes (like methylene blue). A photocatalyst is a substance that, when exposed to charged particles such as electrons and holes, goes through oxidation and reduction reactions on its surface. This process produces additional species that aid in the breakdown of dyes in a solution (Xu *et al.* 2002; Ravi *et al.* 2018).

Since semiconductor-based photocatalysts are easily recyclable, they were previously used to degrade organic dyes (Li *et al.* 2009). Both n-type and p-type semiconductors have photocatalytic properties. It was formerly possible to use TiO_2 (3.2 eV band gap) and ZnO (3.4 eV band gap) efficiently, though their wide band gaps limited their efficiency. Materials capable of absorbing visible light have gained more attention than materials capable of absorbing UV light because of their narrow band gaps (2.1 eV) (Shannon *et al.* 1976; Machida *et al.* 2000; Shi *et al.* 2012).

An oxide having a perovskite structure with the general chemical formula ABO_3 is composed of one or more lanthanide metal ions and one or more transition metal ions, where A represents a lanthanide ion of alkaline metal or rare earth. The optimal crystalline structure for perovskite oxides is the cubic phase, characterized by the $Pm^{\bar{3}}m$ space group. In the process of creating a cubic perovskite oxide, the smaller cation B is responsible for forming a BO_6 unit when positioned at the centre of the unit cell, whereas the larger cation A occupies the corner of the unit cell. Barium zirconate $BaZrO_3$, a frequently studied wide-band-gap perovskite oxide, shows potential for various applications due to its notable electrical conductivity and capacity to accommodate diverse dopants within its crystal structure.

Since $BaZrO_3$ has a large band gap, it can only 4–7% makes up ultraviolet light owing to its lack of crystal defects. Furthermore, oxide vacancies may be deliberately incorporated into the lattice of wide-band-gap materials to enhance their capacity to absorb visible light, or by introducing doping agents consisting of diverse metals or ions. Oxygen vacancies in oxide semiconductors have been shown in some recent studies to enhance solar light absorption by reducing the band gap and, consequently, the probability of photogenerated charge-carrier recombination. The occurrence of oxygen vacancies on the surface can reduce the probability of electron-hole recombination by acting as trap states for charge carriers generated through photoexcitation (Suzuki *et al.* 2012).

Doping metal ions like yttrium (Y^{3+}), the band gap of $BaZrO_3$ can be further adjusted. The adjustment of the band gap through the introduction of intermediate energy levels between the valence band (VB) and the conduction band (CB) enhances the efficiency of charge generation and separation (Xu *et al.* 2015). By inducing distortions in the crystal structure, the doping of $BaZrO_3$ nanoparticles with rare earth metal ions also reduces the size of the crystallites by decreasing the nucleation rate, which increases the surface area. The occurrence of oxygen vacancies on the surface can reduce the probability of electron-hole recombination by acting as trap states for charge carriers generated through photoexcitation. The enlarged surface area facilitates the adsorption and degradation of additional dye molecules present in an aqueous solution. Zirconium-based nanoparticles exhibit significant potential for utilization in photocatalysis applications due to their extensive surface area, narrow band gap, and capacity to facilitate charge carrier conduction, which serves to mitigate electron-hole recombination. Nevertheless, the mesoporous structure, indirect band-gap semiconductor properties, low band gap, UV light sensitivity, high carrier generation, and prolonged electron-hole recombination time of yttrium (Y^{3+}) doped barium zirconate nanoparticles render them significant for facilitating photocatalytic activity. This work is new due to its superior catalytic performance, novel material combinations, and good photocatalytic results (Kudo *et al.* 2007; Wang *et al.* 2020). The yttrium (Y^{3+})-doped barium zirconate is a great photocatalyst under UV light due to the highest degradation of MB dye.

2. EXPERIMENTAL SECTION

All chemicals were used in their original form without any further purification. Barium chloride ($BaCl_2.2H_2O$, 99+% purity) and zirconium chloride ($ZrOCl_4.2.H_2O$, 99.9% purity) were employed as the precursors for the synthesis of barium zirconate nanoparticles, with sodium hydroxide (Merck, 97.7% purity) serving as the precipitating reagent.

2.1 Synthesis of Nanoparticles of $BaZrO_3$ and Yttrium-Doped $BaZrO_3$

The co-precipitation method was used to form the pure $BaZrO_3$ and $BaZrO_3$ doped with Y3+ions nanoparticles (general formula $Ba_{1-x}Y_xZrO_3$, where x = 0.0, 0.02, 0.04, 0.06). Barium chloride ($BaCl_2.2H_2O$) and zirconium chloride ($ZrOCl_4$) were dissolved in 100 mL of distilled water and allowed to stir magnetically for 30 min at room temperature (Solu.1). In another beaker, a calculated amount of NaOH dissolved in 100 mL of distilled water and mixed for 20 min (Solu. 2). After that, the two solutions were mixed and continuously stirred for one hour. After achieving a uniform solution, the material was dried overnight at 50 ℃in a drying oven and then calcined for two hours at 1100 ℃ in a high-temperature furnace.

In the process of incorporating Y^{3+} into $BaZrO_3$ through doping, various proportions of $Y(NO_3)_2$.$4H_2O$ were introduced into the solution, with subsequent steps mirroring those used in the synthesis of pure $BaZrO_3$ nanoparticles. The synthesized Y^{3+}-doped $BaZrO_3$ nanoparticles were utilized for subsequent analysis and evaluation.

2.2 Characterization of Samples

The crystal structures of the products were analyzed using X-ray diffraction (λ=1.5418 Å) radiation. The images were captured with a scanning electron microscope (SEM, JSM 6460LV). The impact of adding dopants on vibrational frequency was studied using an FTIR spectrometer (KBr pellet method) on a TENSOR 27 Spectrometer. Optical properties were analyzed with UV-Vis double beam spectroscopy (Agilent 8453 UV-Vis spectrophotometer) and the luminescence spectrometer LS-55B from Perkin Elmer was used to measure the emission spectrum of photoluminescence (PL) at room temperature, with a Xenon lamp as the excitation source. The investigation of photo-catalytic reactions was conducted utilizing a commercially available photo-reactor (HEBER Photo-reactor, India).

2.3 Photocatalytic Activity Study

The assessment of photocatalytic efficacy consisted of performing experimental procedures to ascertain the efficiency of degrading MB within an aqueous medium. This assessment was conducted under controlled conditions with exposure to UV light generated by a 500 W Philips lamp equipped with a cutoff filter limiting the wavelength to 400-800 nm.

Cold water was employed to regulate the reaction temperature to ambient levels to prevent the occurrence of a thermal catalytic effect. To establish equilibrium between the adsorption and desorption of MB on the photocatalyst, the suspensions were agitated

using a magnetic stirrer in a light-free environment before UV light exposure. Each experimental run used a reactor to mix 48 mL of deionized water with 2 mL of a stock solution of MB (at a concentration of 0.0006 mg/mL). The MB solution was continuously mixed with 75 mg of $BaZrO_3$ powder using a magnetic stirrer. The degradation of MB was examined by centrifuging the collected samples and measuring the absorption peak intensity of MB at 663 nm compared to its initial intensity (C/C_0) with a spectrophotometer (Butler *et al.* 1978).

3. RESULTS AND DISCUSSIONS

3.1 Structural Analysis

The XRD (Fig. 1a) pattern reveals the samples synthesized using the co-precipitation method display a series of distinct and sharp peaks within diffraction angles ranging from 20° to 80°. The peaks are perfectly aligned at 2θ values of 30.2°, 38°, 43°, 48°, 53°, 62°, 70°, and 75°, matching up with crystallographic planes (1 1 0), (1 1 1), (2 0 0), (0 1 2), (2 1 1), (2 2 0), (0 1 3), and (3 1 1) in that order. The X-ray diffraction pattern matches the JCPDS standard No. 06-0399, confirming that the structure of $BaZrO_3$ is indeed perovskite-type cubic with space group $Pm^{-3}m$. Each sample displays diffraction patterns indicative of a single-phase composition of perovskite $BaZrO_3$. As the Y ratio increased, the main peak of the (1 1 0) reflection consistently moved towards lower 2θ angles, ultimately positioning itself between $BaZrO_3$ (Fig. 1b) (Kanhere *et al.* 2011). Despite the high doping concentration of Y^{3+} reaching up to a value of x = 0.06, only a cubic product was formed as a result of the presence of an ample amount of oxygen vacancies. Nevertheless, a noticeable rise in peak intensity is noted in samples with greater Y^{3+} content, indicating a higher degree of crystallinity in the prepared samples (Asahi *et al.* 2001).

With the use of Williamson-Hall (W-H) plots and Scherer's constant formula adjusted for micro-strain, the mean crystallite dimensions (D) of each of the samples were ascertained by analyzing the peak broadening in the X-ray diffraction patterns. To determine the angle θ at which maximum intensity and full width at half maximum (FWHM or β) are achieved, all peaks were subjected to fitting analysis using the Lorentzian curve model. The instrumental broadening (b) was modified according to the prescribed formula;

$$\beta = \beta_{obs} - \beta_{ins} \qquad \ldots\ldots (1)$$

β_{obs} represents the full width at half maximum (FWHM) as determined from the X-ray diffraction (XRD) pattern, while βins refers to the FWHM of the standard sample utilized in the analysis. For the Lorentzian peak shape:

$$\beta \cos\theta = \frac{K\lambda}{D} + 4\varepsilon \sin\theta \qquad \ldots\ldots (2)$$

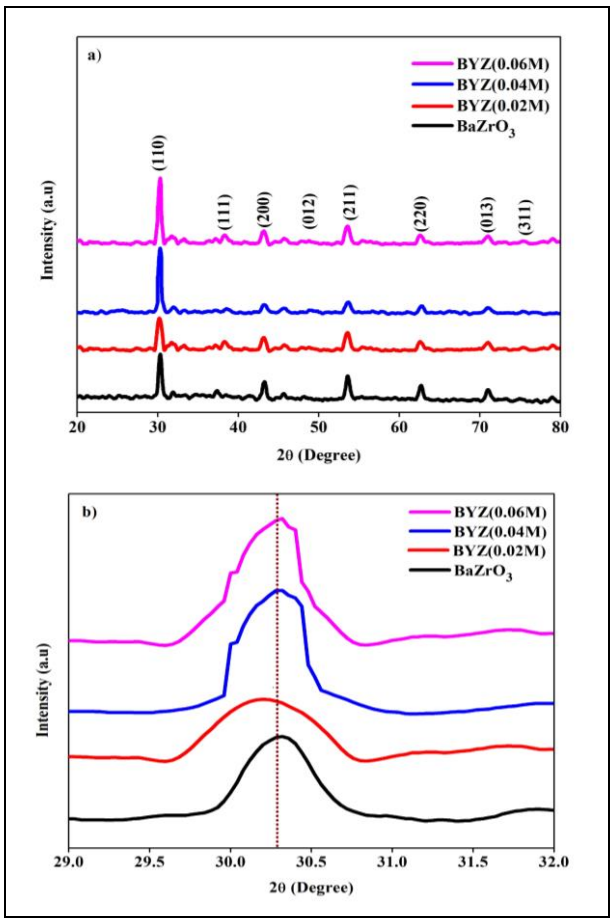

Fig. 1: (a) X-ray diffraction patterns of $Ba_{1-x}Y_x ZrO_3$ (x = 0.0, 0.02, 0.04, 0.06) (b) An enlarged sight of 2θ=29°–32°

In the context of crystal imperfections, ε represents the level of strain present, with λ denoting the X-ray wavelength at a fixed value of 0.154 Å. By plotting β cosθ against 4sinθ, the gradient of the best-fit linear regression line provides a direct measure of the lattice strain, as outlined in the W-H analysis provided in Table 1. As indicated by the graph, the average size of crystallites (D) can be determined by identifying the intercept of the line.

$$D = \frac{\lambda}{\text{intercept}} \qquad \ldots\ldots (3)$$

Table 1 shows that the average size of the crystallites were found to fall between 24 - 35 nm. The observational lattice size for each sample was established through the aggregation of all reflections and the utilization of the Nelson-Riley (N-R) extrapolation method. The N-R function was plotted against the experimental lattice parameter values of each reflected plane.

$$F(\theta) = \frac{1}{2}\left[\left(\frac{\cos^2\theta}{\text{Sin}\,\theta}\right) + \left(\frac{\cos^2\theta}{\theta}\right)\right] \qquad \ldots\ldots (4)$$

θ symbolizes the angle of incidence associated with Bragg's law in crystallography. The lattice parameter values were precisely determined by extending these linear relationships to the points where either F(θ) equals zero or when θ reaches 90° (Yu *et al.* 2003; Hu *et al.* 2017). The lattice parameter (a) values are listed in the table for reference. According to Vegard's law, it has been observed that a rise in the Y^{3+} content causes a linear decrease in the lattice parameter. The alteration in thelattice parameter of iron content is largely influenced by the comparatively reduced ionic radius of Y^{3+}ions (0.1011Å), resulting in their displacement of Zr4+ ions (0.72 Å) when substituted on the B-site within the lattice structure. The pure $BaZrO_3$ sample measures at a = 4.1932 Å, exhibiting a lattice parameter that is in close agreement with values reported in previous studies (Suzuki *et al.* 2012; Grewe *et al.* 2014). Its crystal structure is defined by right angles (a = b = γ = 90°) and equal side lengths.

Table 1. The lattice parameter, average crystallite size, micro-strain, and the distance between 110 planes

Name of Nanoparticles	Value of Lattice parameters a (Å)	Crystalline size (nm) (D)	Lattice strain (ε) ($\times 10^{-3}$)	k (N/cm)	d-spacing (nm)
X=0.0	4.1932	35.6	3.21	2.542	3.02
X = 0.02	4.1926	30.2	1.47	2.680	2.95
X = 0.04	4.1812	32.5	1.52	2.713	2.94
X = 0.06	4.1756	24.5	3.10	2.715	2.96

3.2 Morphological Analysis

The samples were examined using FESEM for their morphologies. The morphological images of the samples with x = 0.00, 0.02, 0.04, and 0.06 are displayed in Fig.2 (a-d), respectively, and they show well-distributed crystallites and dense nanoparticle surfaces. The samples have plenty of pores between the grains and a structure resembling a rod. For each sample, the average grain size (G) was calculated using the linear intercept method using the SEM images (Suzuki *et al.* 2012). The estimated average crystallite size determined from the W-H relation is consistent with an FE-SEM micrograph, and is beneficial to the improvement of photocatalytic activity because it decreases the recombination of photoinduced carriers and increases the number of redox reactions (Xu *et al.* 2002).

3.3 Analysis of FT-IR Spectra

The Fourier-transform infrared spectroscopy spectra of $BaZrO_3$ nanoparticles doped with yttrium are shown in (Fig 3). The stretching vibrations of the Zr-O octahedral are thought to be the source of the dominant peak seen between 550 and 650 cm^{-1}. The notable absorption bands observed are indicative of metal-oxygen stretching vibration at the B site of ABO_3 perovskites, according to the literature currently available (Quéré *et al.* 2004). Thus, the band observed is the consequence of the antisymmetric stretching of $[ZrO_6]$ clusters within a cubic lattice of barium zirconate due to the arrangement of zirconium atoms in octahedral coordination. When compared to the undoped $BaZrO_3$ material, the prominent peak at 1446 cm^{-1} is attributed to the vibrational modes of zirconate (ZrO_3) species (Murphy *et al.* 2002). As the concentration of Y^{3+} increased, there was a noticeable shift in the absorption band in question. This phenomenon arises from the decrease in Zr-O bond length near the Zr substitution site, leading to an alteration in the crystal lattice towards an antisymmetric structure upon substitution of Y^{3+}. The observation indicates a reduction in the Zr-O bond length with the disruption of symmetry. The peaks observed at approximately 1767 cm^{-1}, 2486 cm^{-1}, and 2887 cm^{-1} can be attributed to the stretching and bending vibrations of the hydroxyl (O-H) functional group, in agreement with previous studies on hydroxyl ($^{-}$OH) species.

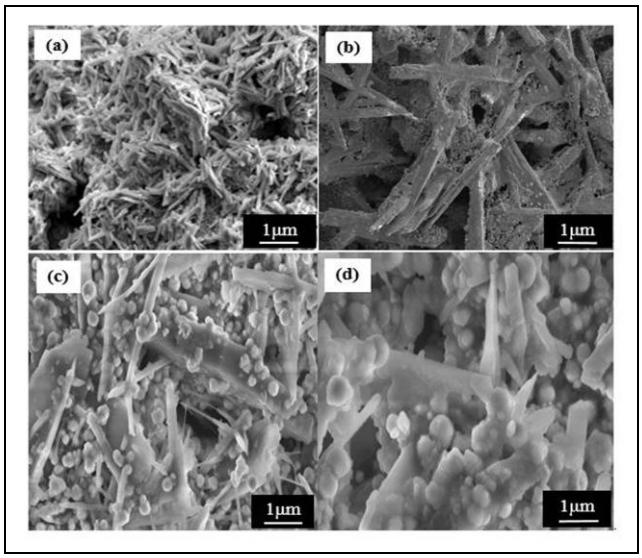

Fig. 2: Morphology images of $Ba_{1-x}Y_x ZrO_3$ (x =0.0, 0.02, 0.04, 0.06)

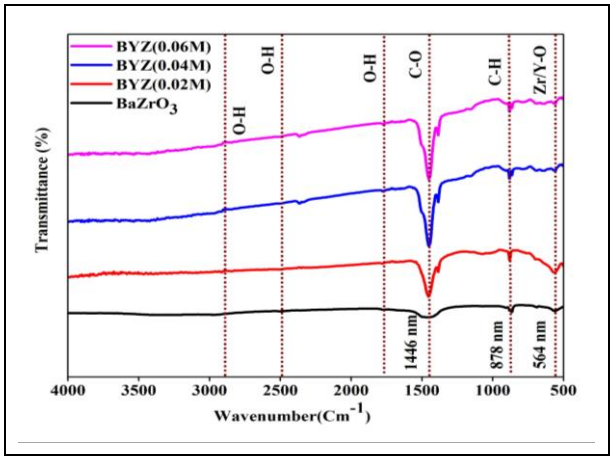

Fig. 3: FT-IR spectra of $Ba_{1-x}Y_x ZrO_3$ (x = 0.0, 0.02, 0.04, 0.06)

These bands consist of dimers bonded through intermolecular interactions with hydroxyl groups. The addition of base can cause slight movement of these dimers within the reaction medium. The findings of our study on pure $BaZrO_3$ nanoparticles closely align with the data documented in previous studies (Quéré *et al.* 2004; Mizoguchi *et al.* 2004). The FT-IR spectra clearly show that the Y-doped $BaZrO_3$ samples do not exhibit any extra peaks. Instead, there is a noticeable shift in the bands as the concentration of Y increases.

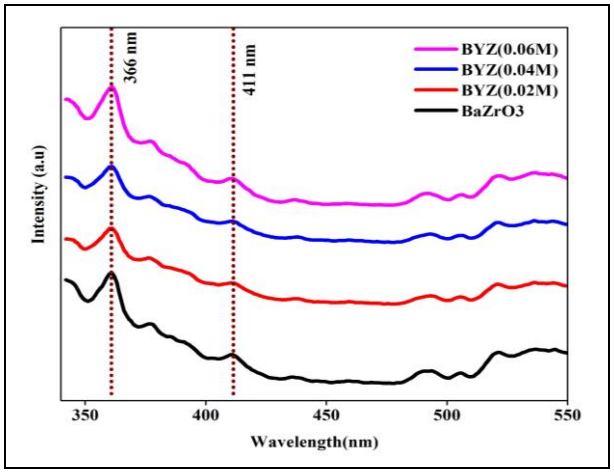

Fig. 4: PL emission spectra of $Ba_{1-x}Y_x ZrO_3$ (x = 0.0, 0.02, 0.04, 0.06)

3.4 Photoluminescence Spectra

Fig. 4 displays the emission spectra of the samples at a wavelength of 300 nm. The prepared samples exhibit a significant emission in the blue and violet regions, with peak wavelengths of approximately 366 nm and 411 nm, respectively. The PL profile clearly shows that as the concentration of Y increases, the excitation centres of the samples at 366 nm and 411 nm decrease and become insignificant. This is especially noticeable in the x = 0.06 sample. The phenomenon under observation could be explained by a reduction in disorder brought about by the stabilizing effect of the increasing quantity of Y3þ–Y4þ exchange pairs.

A notable blue-violet photoluminescence emission stemming from oxygen vacancies was detected in submicron crystals of $BaZrO_3$ polyhedrons. Based on the empirical findings, it is hypothesized that the photoluminescence mechanism observed in this study may be attributed to the formation of defects arising from oxygen exhaustion during the annealing process, leading to the rupture of Zr-O bonds and the introduction of impurities. The presence of Y^{3+} ions leads to the promotion of defects within the system due to disparities in ionic size and the need for charge compensation arising from variations in electron valence between the dopant and the substituted ion. Notably, the dopants under investigation exhibit varying levels of influence on the system (Butler *et al.* 1978; Scaife *et al.* 1980; Suzuki *et al.* 2012).

3.5 UV-vis Absorption Spectroscopy

The UV-visible absorption spectra of Y-doped $BaZrO_3$ were analysed to investigate the optical characteristics of photocatalysts, as illustrated in the corresponding (Fig. 5a). It is evident that as the concentration of Y^{3+} in the $BaZrO_3$ structure increases, the absorption edge shifts progressively towards longer wavelengths. The Pure $BaZrO_3$ has a band energy of approximately 3.60 eV as estimated from the Tauc's plot in (Fig. 5b). The optical band gap energy can be evaluated utilizing the Tauc's relation

as depicted in the following equation:

$$(\alpha h\upsilon) = B\,(h\upsilon - E_g)^n \qquad \ldots\ldots\ldots (5)$$

Eq. 5 uses the following notations: α stands for the material's linear absorption coefficient, B for the constant of proportionality, 'h' for Planck's constant (6.6260×10^{-34} Js), n for photon energy, and Eg for the optical energy band gap, and the constant n corresponds to various types of electronic transitions (for direct allowed transitions n=0.5, for an indirect allowed transition n=2, for a forbidden transition n=1.5, and an indirect forbidden transition n=3). The values of Eg for the nanoparticles synthesized were determined using the value of n=2 in Equ. 5. The optical energy band gap can be determined by identifying the point at which the linear portion of the curve representing $(\alpha h\upsilon)^2$ plotted on the Y-axis intersects with the energy of the photon ($h\upsilon$) on the X-axis, as illustrated in (Fig. 5b).

The pure $BaZrO_3$ material demonstrates an optical band gap of 3.60 eV, a value that closely aligns with that documented in previous literature (Butler *et al.* 1978). The decrease in band gap energy with increasing concentration of element Y was explained by the rise in lattice defects, resulting in higher levels of intermediary energy within the band gap region of disordered $BaZr_{1-x}Fe_xO_3$ nanoparticles. After the introduction of dopants, there is a reduction in the band gap, with the band gap value diminishing incrementally as the concentration of Y(x=0.06) doping content increases. In our experiment, $BaZrO_3$ samples with varying levels of Y doping (x=0.02, 0.04, 0.06) exhibited an increase in unit cell volume as the concentration of Y decreased. This resulted in a local straightening of the Zr-O-Zr bond angle within the structure, ultimately reducing the band gap. The concentration of Y-doped $BaZrO_3$ at x=0.06 exhibits a higher absorption capacity and a longer absorption band edge wavelength compared to pure $BaZrO_3$. Incorporating Y doping at x=0.06 causes impurity energy levels to form within the band gap, which moves the acceptor energy level below the original conduction band or the donor energy level above the

original valence band. At x=0.06, this modification decreases the band gap energy (Eg) of Y-doped $BaZrO_3$. The efficiency of photocatalysis increases with a decrease in the band gap (Butler *et al.* 1978; Scaife *et al.* 1980).

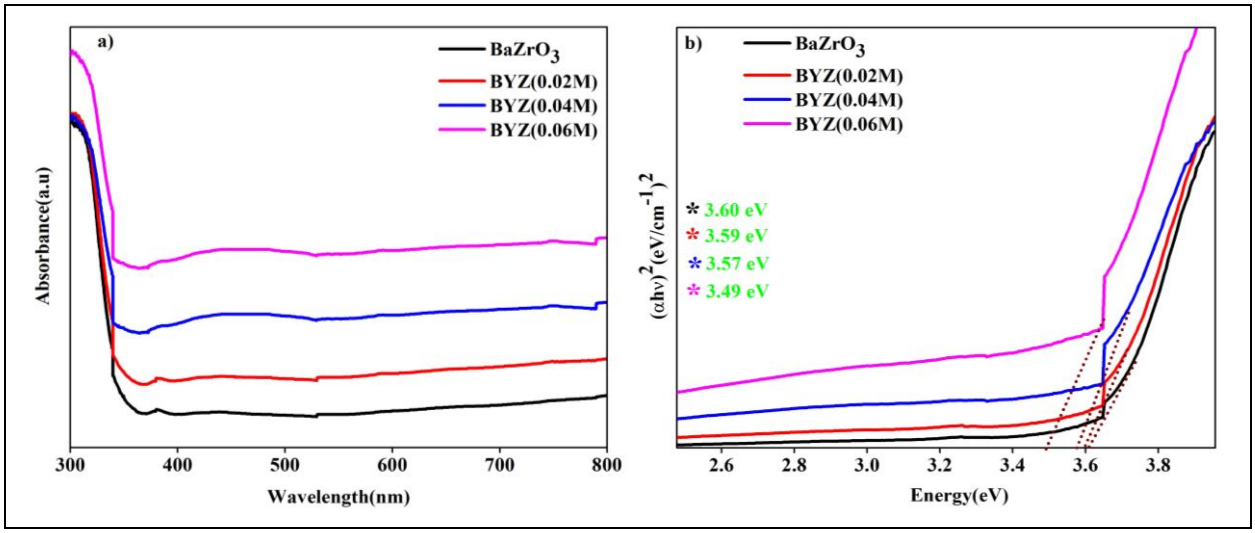

Fig. 5: (a) UV-Vis absorption spectra of $Ba_{1-x}Y_xZrO_3$ (b) Tauc's plot for $Ba_{1-x}Y_xZrO_3$

3.6 Photocatalytic Efficiency in the Degradation of MB dye

The photocatalytic properties of pure $BaZrO_3$ and Y-doped $BaZrO_3$ materials towards the degradation of methylene blue dye under UV light exposure were examined.

3.6.1 Optimization of Parameters

In order to achieve the highest effectiveness in breaking down MB dye through photo-oxidative degradation under visible light, experiments were conducted to optimize various parameters including the pH of the reaction solution, the amount of catalyst, and the initial concentration of the dye. This optimization process was carried out using both a pure $BaZrO_3$ catalyst and a various concentration of Y-doped $BaZrO_3$.

3.6.2 Photocatalytic Performance of $BaZrO_3$ and Different Concentration of Y-doped $BaZrO_3$

The $BaZrO_3$ and Y-doped nanoparticles, synthesized at varying doping levels (x=0.02, 0.04, 0.06) have been demonstrated to degrade organic dyes frequently encountered in industrial wastewater effectively. In this study, the degradation efficiency was evaluated by selecting MB as the representative system. In order to achieve this objective, two experiments were conducted under contrasting conditions of darkness and illumination. During the experiment conducted in the absence of light, the catalytic solution was supplemented with MB. Consequently, the absence of charge carrier formation, specifically electrons and holes, leads to the absence of dye degradation. The noteworthy emergence of the dark effect can be attributed to adsorption, an inevitable phenomenon. The role of light-induced experiments is significant in the degradation of dyes due to the generation of charge carriers. For the light experiment, an initial concentration of MB was generated by combining 2 mL of an MB stock solution (with a concentration of 0.0006 mg/mL) with 48 mL of deionized water. The MB solution was supplemented with 75 mg of each catalyst (Mizoguchi *et al.* 2004). To establish a stable equilibrium between the photocatalyst and the organic compound, the dye solutions containing catalysts were thoroughly mixed in darkness for 30 min prior to exposure to light. The absorption of MB significantly diminished following exposure to visible light.

This suggests that the breakdown of MB took place, thereby impeding any additional adsorption. Spectral analysis necessitated the collection of aliquots measuring 3 mL at intervals of 30 min. A prominent peak around 663 nm was visible in the absorption spectrum of MB, as shown in Fig. 6 (a-d) (Zhou *et al.* 2015). (Fig 6d) depicts the breakdown of MB dye in a solution with a pH of 8, utilizing the most effective concentration of x=0.06. A gradual decrease in peak intensity at a wavelength of 663 nm of MB was observed through continuous monitoring. In 2 hours, the intensity decreased to a point greater than 98.5%. The effectiveness of the samples was evaluated by employing the equation provided below equ.6.

$$\text{Degradation } (\%) = \frac{C_0 - C}{C} \times 100 \quad \ldots\ldots (6)$$

C_0 denotes the dye solution's initial concentration, and its concentration at a given time t is represented by C. The percentage degradation efficiency

of $BaZrO_3$ and $Ba_{1-x}Y_xZrO_3$ nanoparticles (where x = 0.02, 0.04, and 0.06) is shown graphically in (Fig 7). The research indicates the nanoparticles with a concentration of X=0.06 exhibits the highest degradation efficiency of ~98.5% when compared to pure $BaZrO_3$, Y-doped concentrations at x=0.02, x=0.04 which show degradation efficiencies of approximately 56.7%, 65.3%, and 78.9%, respectively. The increase in the efficiency of dye degradation by BYZ (0.06) nanoparticles relative to pure $BaZrO_3$ may be attributed to the nanoparticle's improved light absorption and superior ability to transfer charge (Mizoguchi *et al.* 2004).

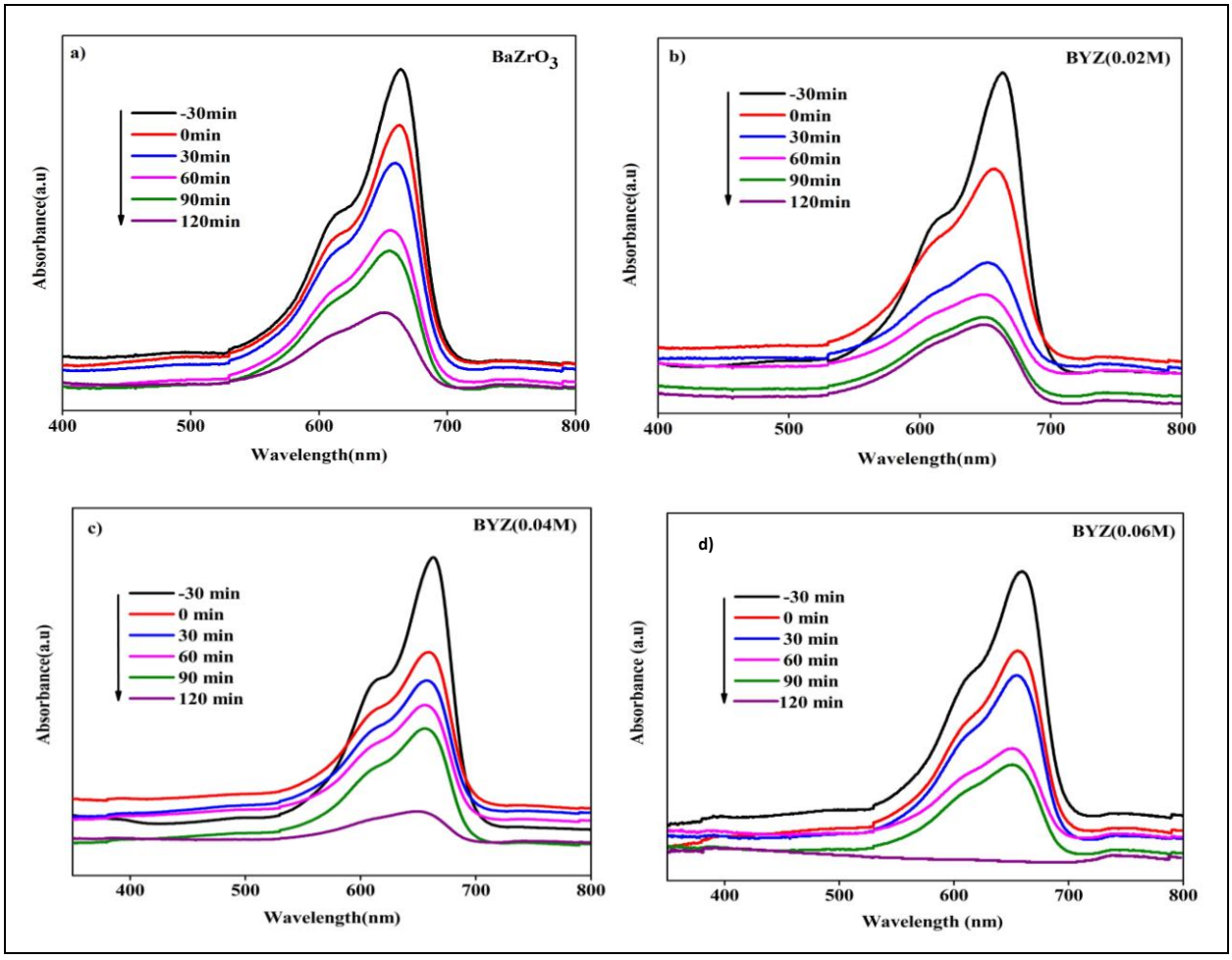

Fig. 6 (a-d): Photocatalytic degradation of methylene blue dye by $Ba_{1-x}Y_xZrO_3$

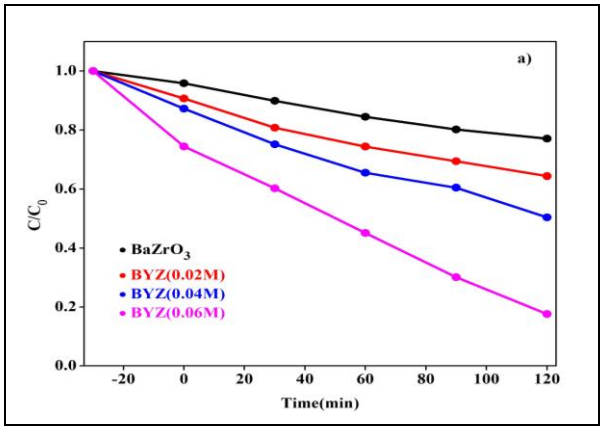

Fig. 7: Photocatalytic degradation percentages of MB dye at the end of 120 min by $Ba_{1-x}Y_x$ ZrO_3 nanoparticles

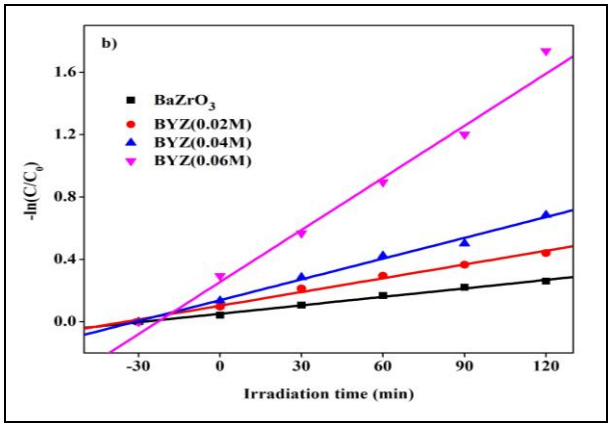

Fig. 8: The graph of $ln(C_0/C)$ as a function of time over $Ba_{1-x}Y_x$

3.6.3 Kinetics Studies

The kinetics of photocatalytic reactions are characterized by the Langmuir-Hinshelwood (L-H) equations, which is represented by the formula below.

$$\text{First order (n=1): } \ln\left(\frac{C_0}{C}\right) = kt \quad \ldots (7)$$

In this context, k represents the pseudo-first-order rate constant in units of (min^{-1}), while C0 denotes the initial various time intervals denoted by t (Kato *et al.* 2003). In the case of $Ba_{1-x}Y_xZrO_3$ (x =0.0, 0.02, 0.04, 0.06) compounds, analysis of the relationship between the natural logarithm of the initial concentration of MB solution relative to its concentration at time t (ln(C0/C)) and irradiation time (t) revealed that the degradation of MB through photocatalysis followed a first-order kinetics mechanism.

The degradation rate constants (k) can be computed by looking at the t plot's slope versus $\ln(C_0/C)$. As seen in (Fig. 8), BYZ (0.06) exhibits the highest degradation rate constant of all the compounds. The sequencing observed is $BaZrO_3$ (k=0.00181 min^{-1}) exhibiting the highest reaction rate followed by BYZ (0.02) (k=0.00294 min^{-1}) and BYZ (0.04) (k=0.00444 min^{-1}), as indicated by the regression coefficients R2=0.993, R2=0.988, R2=0.992, and R2=0.9 (Murase *et al.* 2004).

3.6.4 Stability of catalysts and studying the photocatalytic cycle

Degrading MB was done in five different cycles to evaluate the photocatalyst's stability and reusability for repeated use. The standard UV-light absorption data of MB on BYZ (0.06) catalyst and the rends of degradation over five consecutive catalytic cycles are shown in (Fig 9a).

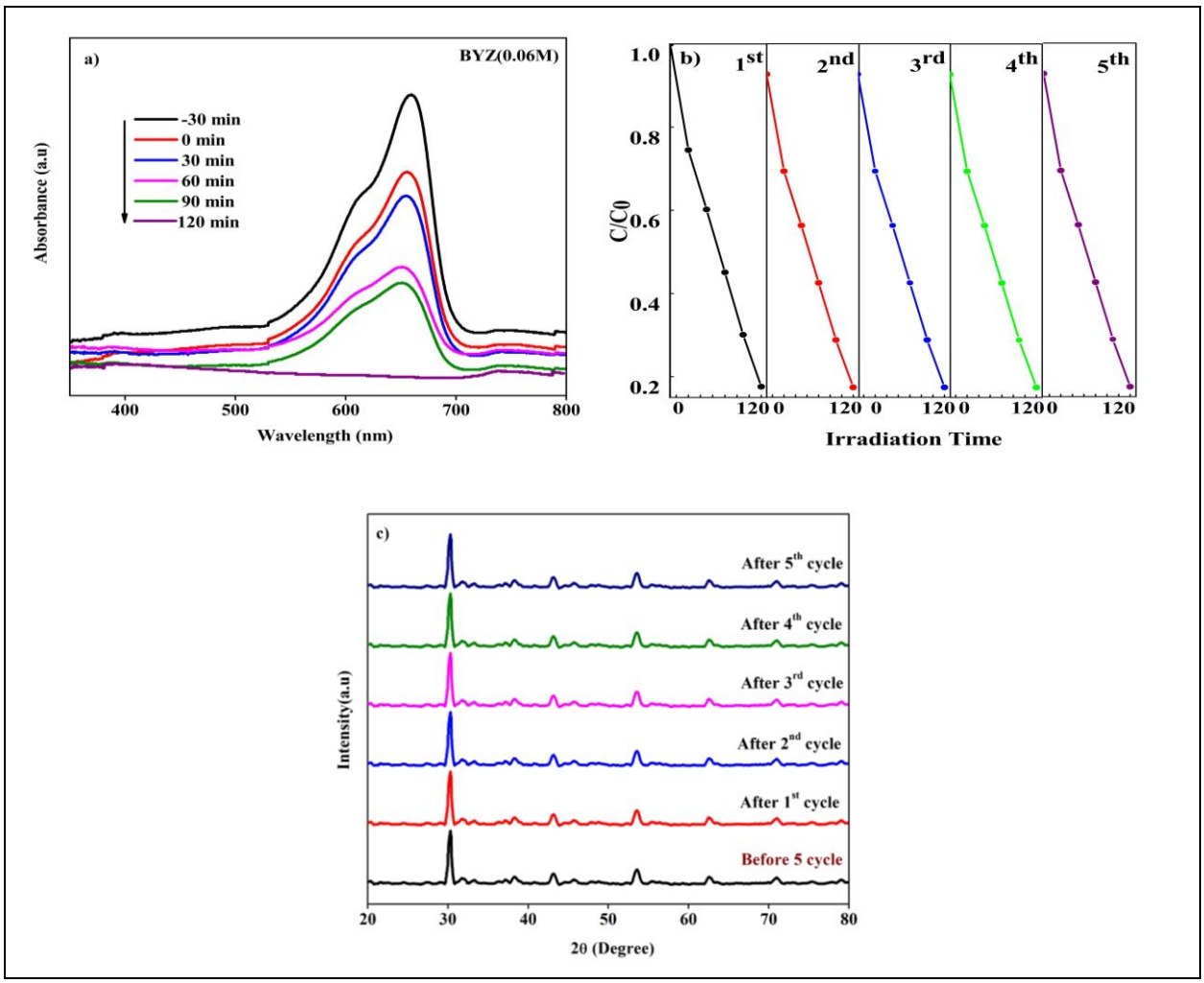

Fig. 9: (a) The absorption spectra of MB under UV light change as the irradiation time increases with a concentration of BYZ (0.06) (b) The ability for the BYZ (0.06) phase to be used for reusability and stability in the photocatalytic degradation of MB over five successive trials (c) X-ray diffraction patterns of BYZ (0.06) before and after five cycles of degrading MB through photocatalysis

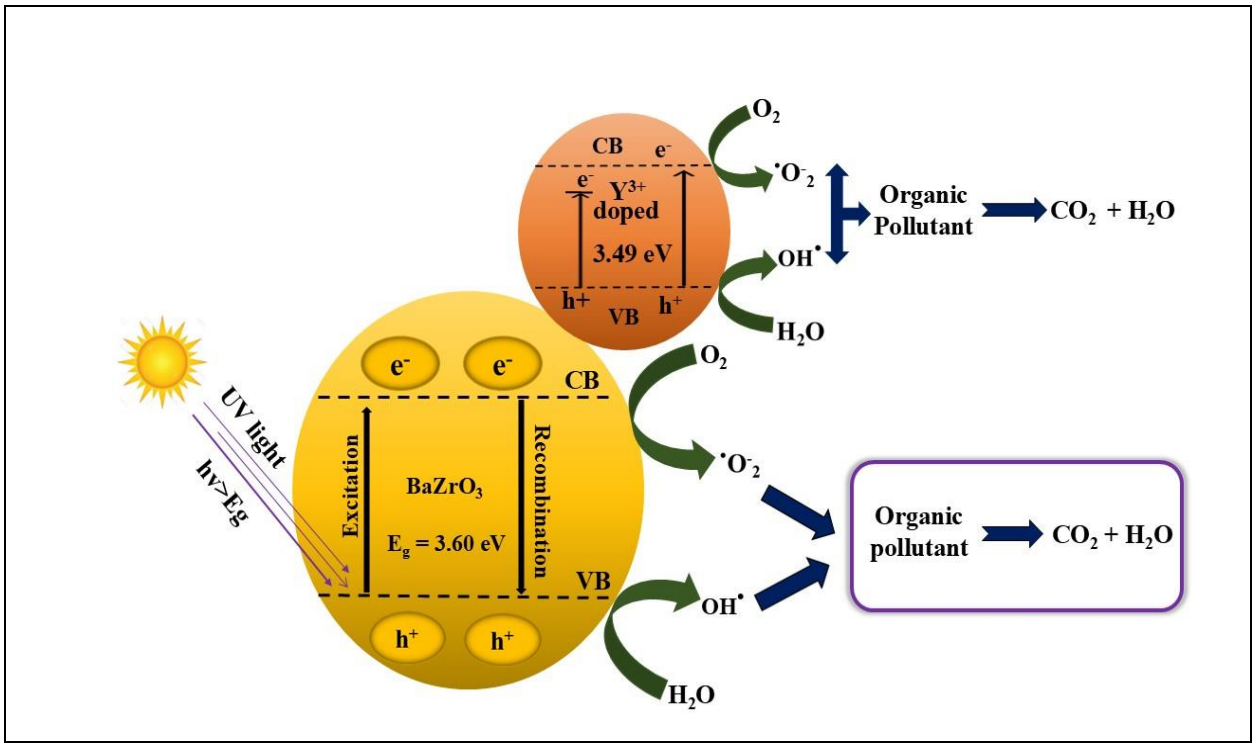

Fig. 10: Schematic process of charge transfer during the photodegradation of methylene blue dye by $Ba_{1-x}Y_xZrO_3$ nanoparticles when exposed to UV light

The $BaZrO_3$-based photocatalyst displaying the most superior photocatalytic performance, as measured by BYZ (0.06) in (Fig 9b), was chosen for the photocatalytic cycle test due to its stability. The data obtained from the experiment indicates that the photocatalytic efficiency of the sample with x=0.06 powder exhibits minimal deterioration in its ability to degrade the MB dye solution following its second regeneration. Even after undergoing five cycles, there was no significant decrease in catalytic efficiency and the degradation rate remained at 98.5%, suggesting that the sample exhibited excellent stability and was suitable for extended usage in the degradation of organic pollutants. Fig. 9c shows the X-ray diffraction (XRD) patterns for BYZ (0.06) catalysts after the fifth cycle. There was no indication of phase separation or photo corrosion during the dye degradation, according to the X-ray diffraction (XRD) analysis, which also turned up no evidence of impurities from decomposition.

Moreover, the catalysts after degradation were found to retain a significant level of crystallinity, indicating remarkable stability and longevity of the catalysts under the reaction conditions (Murase *et al.* 2004; Rao *et al.* 2018).

3.6.5 Mechanistic Insights for Enhanced Photocatalytic Activity

The diagram in Fig.10 depicts the schematic mechanism of the photocatalysis process. The process of heterogeneous photocatalysis in semiconductor materials commences with photoexcitation induced by the interaction of light with the semiconductor material. To facilitate the movement of electrons from the valence band to the conduction band and generate a hole in the valence band, known as an electron-hole pair, the magnitude of energy of the light source must surpass or equal the bandgap energy threshold (Equ.8). The oxidation-reduction reaction commences with the introduction of adsorbed compounds on the surface of the semiconductor. A suitable scavenger will transfer the electron-hole pair to inhibit its recombination, as outlined in Eq. 9.

While the positive hole in the valence band will join with the electron donor, the electron in the conduction band will combine with the electron acceptor. When electron donors experience oxidation throughout the electron transfer process, electron acceptors, typically O_2, are reduced to other molecules. The redox mechanism is employed for mitigating contaminants that interact with the surface of the photocatalyst. Electrons and holes can generate active radicals which can be utilized in the degradation of pollutants. Electrons will engage in interactions with either air or oxygen to generate superoxide radicals ($\bullet O_2^-$) according to Equ.10. On the other hand, when holes come into contact with water molecules (H_2O), they combine to produce hydroxyl radicals (OH•) (Equ.11). Superoxide radicals may undergo a process by which they are transformed

into hydrogen peroxide, involving the formation of hydroperoxyl radicals. Hydrogen peroxide may undergo conversion to hydroxyl radical when exposed to light, specifically ultraviolet light, as described in Equ.14. These reactive species (hydroxyl radical, superoxide radical, and hydrogen peroxide) are responsible for breaking down pollutant compounds into simpler molecules like carbon dioxide (CO_2), H_2O, and mineral acids according to Equ.15 referenced in literature.

$$BaZrO_3 + hv \rightarrow BaZrO_3 (e_{CB}^- + h_{VB}^+) \quad \ldots (8)$$

$$aZrO_3 (e_{CB}^- + h_{VB}^+) \rightarrow BaZrO_3 + heat \quad \ldots (9)$$

$$e_{CB}^- + O_2 \rightarrow \bullet O_2^- \quad \ldots (10)$$

$$h_{VB}^+ + H_2O \rightarrow OH\bullet + H^+ \quad \ldots (11)$$

$$\bullet O_2^- + H^+ \rightarrow \bullet OOH \quad \ldots (12)$$

$$2\bullet OOH \rightarrow O_2 + H_2O_2 \quad \ldots (13)$$

$$H_2O_2 + hv \rightarrow 2OH\bullet \quad \ldots (14)$$

$$\text{Pollutant} + (OH\bullet, \bullet O_2^-) \rightarrow CO_2 + H_2O \text{ (degraded product)} \quad \ldots (15)$$

In the case of heterogeneous photocatalysis, the comprehensive sequence of events can be categorized into five distinct stages: (i) The movement of liquid-phase reactants towards the surface of the catalyst; (ii) The binding of reactants to the catalyst surface induced by photons; (iii) The commencement of photocatalytic reactions within the adsorbed phase on the catalyst surface; (iv) The emission of substances/products from the catalyst surface through desorption; (v) The segregation and conveyance of substance/product mass from the interface region (Kato *et al.* 2003; Murase *et al.* 2004).

4. CONCLUSION

In summary, the research showed that $Ba_{1-x}Y_xZrO_3$ (x=0.0, 0.02, 0.04, 0.06) perovskite nanoparticles were effectively synthesized to break down MB dye through photocatalysis. The $Ba_{1-x}Y_xZrO_3$ samples prepared have a narrow bandgap of 3.49 eV, allowing them to be effectively used under UV-visible light exposure. The $Ba_{1-x}Y_xZrO_3$ photocatalyst showed a high photocatalytic efficiency of 98.5% in degrading (0.0006 mg/mL) MB dye after 120 min using a UV light source. The enhanced photocatalytic performance of the BYZ (0.06) catalyst can be primarily attributed to a reduction in electron-hole charge recombination, improved UV-light absorption capacity, enhanced electron mobility, and remarkable catalytic properties.The parameters to minimize the amount of time needed to machine Inconel 625 were: current (12 A), pulse on time (70 µs), and pulse off time (90 µs).

FUNDING

This research received no specific grant from any funding agency in the public, commercial, or not-for-profit sectors.

CONFLICTS OF INTEREST

The authors declare that there is no conflict of interest.

REFERENCES

Asahi, R., Morikawa, T., Ohwaki, T., Aoki, K. and Taga, Y., Visible-Light Photocatalysis in Nitrogen-Doped Titanium Oxides, *Sci.*, 293(5528), 269–271 (2001). https://doi.org/10.1126/science.1061051

Butler, M. A. and Ginley, D. S., Prediction of Flatband Potentials at Semiconductor-Electrolyte Interfaces from Atomic Electronegativities, *J. Electrochem. Soc.*, 125(2), 228–232 (1978). https://doi.org/10.1149/1.2131419

Fujishima, A. and Honda, K., Electrochemical Photolysis of Water at a Semiconductor Electrode, *Nature*, 238(5358), 37–38 (1972). https://doi.org/10.1038/238037a0

Grewe, T., Meier, K. and Tüysüz, H., Photocatalytic hydrogen production over various sodium tantalates, *Catal. Today*, 225, 142–148 (2014). https://doi.org/10.1016/j.cattod.2013.10.092

Hu, C.-C., Huang, H.-H. and Huang, Y.-C., N-doped NaTaO 3 synthesized from a hydrothermal method for photocatalytic water splitting under visible light irradiation, *J. Energy Chem.*, 26(3), 515–521 (2017). https://doi.org/10.1016/j.jechem.2016.12.002

Kanhere, P. D., Zheng, J. and Chen, Z., Site Specific Optical and Photocatalytic Properties of Bi-Doped NaTaO 3, *J. Phys. Chem. C*, 115(23), 11846–11853 (2011). https://doi.org/10.1021/jp2003936

Kato, H. and Kudo, A., Photocatalytic water splitting into H2 and O2 over various tantalate photocatalysts, *Catal. Today*, 78(1–4), 561–569 (2003). https://doi.org/10.1016/S0920-5861(02)00355-3

Kudo, A., Photocatalysis and solar hydrogen production, *Pure Appl. Chem.*, 79(11), 1917–1927 (2007). https://doi.org/10.1351/pac200779111917

Li, X. and Zang, J., Facile Hydrothermal Synthesis of Sodium Tantalate (NaTaO3) Nanocubes and High Photocatalytic Properties, *J. Phys. Chem. C*, 113(45), 19411–19418 (2009). https://doi.org/10.1021/jp907334z

Machida, M., Yabunaka, J. and Kijima, T., Synthesis and Photocatalytic Property of Layered Perovskite Tantalates, RbLnTa 2 O 7 (Ln = La, Pr, Nd, and Sm), *Chem. Mater.*, 12(3), 812–817 (2000). https://doi.org/10.1021/cm990577j

Mizoguchi, H., Eng, H. W. and Woodward, P. M., Probing the Electronic Structures of Ternary Perovskite and Pyrochlore Oxides Containing Sn 4+ or Sb 5+, *Inorg. Chem.*, 43(5), 1667–1680 (2004). https://doi.org/10.1021/ic034551c

Murase, T., Irie, H. and Hashimoto, K., Visible Light Sensitive Photocatalysts, Nitrogen-Doped Ta 2 O 5 Powders, *J. Phys. Chem. B*, 108(40), 15803–15807 (2004). https://doi.org/10.1021/jp047874i

Murphy, C. J., Nanocubes and Nanoboxes, *Sci.*, 298(5601), 2139–2141 (2002). https://doi.org/10.1126/science.1080007

Quéré, D., di Meglio, J.-M. and Brochard-Wyart, F., Spreading of Liquids on Highly Curved Surfaces, *Sci.*, 249(4974), 1256–1260 (1990). https://doi.org/10.1126/science.249.4974.1256

Rao, M. P., Nandhini, V. P., Wu, J. J., Syed, A., Ameen, F. and Anandan, S., Synthesis of N-doped potassium tantalate perovskite material for environmental applications, *J. Solid State Chem.*, 258, 647–655 (2018). https://doi.org/10.1016/j.jssc.2017.11.031

Ravi, P., Navakoteswara Rao, V., Shankar, M. V. and Sathish, M., CuO Cr 2 O 3 core-shell structured co-catalysts on TiO 2 for efficient photocatalytic water splitting using direct solar light, *Int. J. Hydrogen Energy*, 43(8), 3976–3987 (2018). https://doi.org/10.1016/j.ijhydene.2017.08.213

Scaife, D. E., Oxide semiconductors in photoelectrochemical conversion of solar energy, *Sol. Energy*, 25(1), 41–54 (1980). https://doi.org/10.1016/0038-092X(80)90405-3

Shannon, R. D., Revised effective ionic radii and systematic studies of interatomic distances in halides and chalcogenides, *Acta Crystallogr. Sect. A*, 32(5), 751–767 (1976). https://doi.org/10.1107/S0567739476001551

Shi, J., Liu, G., Wang, N. and Li, C., Microwave-assisted hydrothermal synthesis of perovskite NaTaO3 nanocrystals and their photocatalytic properties, *J. Mater. Chem.*, 22(36), 18808 (2012). https://doi.org/10.1039/c2jm33470d

Suzuki, S., Teshima, K., Yubuta, K., Ito, S., Moriya, Y., Takata, T., Shishido, T., Domen, K. and Oishi, S., Direct fabrication and nitridation of a high-quality NaTaO3 crystal layer onto a tantalum substrate, *CrystEngComm*, 14(21), 7178 (2012). https://doi.org/10.1039/c2ce25901j

Wang, Q. and Domen, K., Particulate Photocatalysts for Light-Driven Water Splitting: Mechanisms, Challenges, and Design Strategies, *Chem. Rev.*, 120(2), 919–985 (2020). https://doi.org/10.1021/acs.chemrev.9b00201

Xu, D., Yang, S., Jin, Y., Chen, M., Fan, W., Luo, B. and Shi, W., Ag-Decorated ATaO 3 (A = K, Na) Nanocube Plasmonic Photocatalysts with Enhanced Photocatalytic Water-Splitting Properties, *Langmuir*, 31(35), 9694–9699 (2015). https://doi.org/10.1021/acs.langmuir.5b01294

Xu, H. and Gao, L., New evidence of a dissolution–precipitation mechanism in hydrothermal synthesis of barium titanate powders, *Mater. Lett.*, 57(2), 490–494 (2002). https://doi.org/10.1016/S0167-577X(02)00817-0

Yin, W.-J., Weng, B., Ge, J., Sun, Q., Li, Z. and Yan, Y., Oxide perovskites, double perovskites and derivatives for electrocatalysis, photocatalysis, and photovoltaics, *Energy Environ. Sci.*, 12(2), 442–462 (2019). https://doi.org/10.1039/C8EE01574K

Yu, S. -H., Liu, B., Mo, M. -S., Huang, J. -H., Liu, X. -M. and Qian, Y. -T., General Synthesis of Single-Crystal Tungstate Nanorods/Nanowires: A Facile, Low - Temperature Solution Approach, *Adv. Funct. Mater.*, 13(8), 639–647 (2003). https://doi.org/10.1002/adfm.200304373

Yuan, L., Han, C., Yang, M.-Q. and Xu, Y.-J., Photocatalytic water splitting for solar hydrogen generation: fundamentals and recent advancements, *Int. Rev. Phys. Chem.*, 35(1), 1–36 (2016). https://doi.org/10.1080/0144235X.2015.1127027

Zhou, H., Li, P., Guo, J., Yan, R., Fan, T., Zhang, D. and Ye, J., Artificial photosynthesis on tree trunk derived alkaline tantalates with hierarchical anatomy: towards CO 2 photo-fixation into CO and CH 4, *Nanoscale*, 7(1), 113–120 (2015). https://doi.org/10.1039/C4NR03019B